J. Fluid Mech. (1977), *vol.* 80, *part* 3, *pp.* 481–507
Printed in Great Britain

On the evolution of the system of wind drift currents and Langmuir circulations in the ocean. Part 2. Structure of the Langmuir vortices

By S. LEIBOVICH AND K. RADHAKRISHNAN†

Sibley School of Mechanical and Aerospace Engineering, Cornell University, Ithaca, New York 14853

(Received 21 July 1976)

Numerical solutions are presented for the detailed characteristics of the drift current and Langmuir circulation system produced according to a theory described in part 1 of this paper. The motions that develop are traced from an initially quiescent state, and the results are compared with field observations of currents in Langmuir circulations. Qualitative features of the phenomenon appear to be reproduced by the theory and, with the appropriate choice of an empirical parameter, the solutions seem to be quantitatively consistent with field data.

1. Introduction

Langmuir (1938) identified a coherent convective motion in the surface layers of lakes and the oceans in the form of roll cells with axes parallel to the direction of the wind. From his observational studies of these motions, Langmuir concluded that they are mechanical in origin, and that the principal motive force is the applied wind stress. He further speculated that the mixing accomplished by the cells might be the agency responsible for the formation of the thermocline. Craik & Leibovich (1976) listed five features of the Langmuir circulations that they believed to be most firmly established by field observations and that any satisfactory theory presumably must therefore explain: (i) a parallel system of vortices aligned with the wind must be predicted, (ii) a means must be given by which these vortices are driven by the wind, (iii) the resulting cells must have the possibility of an asymmetric structure with down-welling speeds larger than upwelling speeds, (iv) downwelling zones must be under lines where the wind-directed surface current has a maximum, and (v) the Langmuir circulations must have maximum downwelling speeds which are comparable with the mean wind-directed surface drift. These attributes have been consistently reported by observers and may be considered to be commonly accepted features of the phenomenon. Langmuir's observations were extensive, although not entirely systematic. More recent field observations, however, have confirmed Langmuir's description of the structure and origin of these motions.

Two new and distinct theoretical mechanisms in addition to that given by Craik & Leibovich (1976) have been proposed, essentially simultaneously, by Gammelsrød (1975) and by Garrett (1976). These recent efforts were stimulated by a renewed awareness of the important impact Langmuir circulations must have on the dynamics

† Present address: Department of Mechanical Engineering, Massachusetts Institute of Technology.

of the mixed layer in the ocean. The potential significance of the vertical mixing accomplished by the motions discovered by Langmuir has been recently emphasized by Leibovich & Ulrich (1972) and in reports on field observations by Scott *et al.* (1969), Myer (1971), Assaf, Gerard & Gordon (1971) and Gordon (1970). The present paper continues an extension and refinement of the Craik–Leibovich model that was begun in Leibovich (1976). Before describing the contents of the present contribution we will briefly review the theories advanced by Gammelsrød and Garrett.† Craik & Leibovich (1976), which will be referred to as CL below, may be consulted for references to reviews of earlier work, and for additional discussion of the phenomenon. Also, Pollard's (1976) review of the subject summarizes experimental and theoretical efforts, and points to the potential significance of this phenomenon to mixed-layer dynamics.

The theory proposed by Gammelsrød assumes the existence of uniformly sheared current in a mixed layer with depth H small compared with the Ekman depth. In this case, Ekman's classic solution (1905) for finite depth yields a current that is essentially parallel to the wind direction and uniformly sheared, even though the Coriolis acceleration is accounted for. Gammelsrød then considers the linearized stability of this current to roll motions parallel to the current direction. The inclusion of the Coriolis acceleration is crucial, since in its absence no instability occurs. When the dimensionless shear rate $s = f^{-1}\Delta U/H$ is sufficiently large (where ΔU is the basic current variation across the layer with thickness H and f is the Coriolis parameter) Gammelsrød finds that small disturbances will amplify on a time scale consistent with the growth time of Langmuir cells. As an example, observations of wind streaks made in Josenfjorden, Norway, were cited under the following conditions: depth H of the pycnocline was only 2 m, and ΔU was 20 cm/s. Thus, the depth H was small compared with the Ekman depth, as required, and the dimensionless shear rate $s \sim 10^3$ was large. The e-folding time of amplifying disturbances with a streak width of 5 m was computed to be 13 min, which is consistent with Langmuir circulation data.

A significant Coriolis effect is very curious, however, and upon closer examination it seems to us that Gammelsrød's theory is not likely to apply to the phenomenon of Langmuir circulation. Let v be a velocity scale characteristic of the amplifying instability that Gammelsrød identifies as the growing Langmuir circulation, and estimate the Rossby number ϵ_R based upon v and H, so that

$$\epsilon_R = v/fH.$$

Coriolis accelerations are significant compared with inertial effects only when ϵ_R is small. Using the data already cited by Gammelsrød (i.e. $fH = 0{\cdot}02$ cm/s when $s = 10^3$), however, we find that ϵ_R exceeds unity for v in excess of $0{\cdot}02$ cm/s. Thus for motions as vigorous as Langmuir circulations (many cm/s), the Coriolis acceleration essential to the Gammelsrød mechanism is negligible compared with inertial effects. This implies, for us, that Gammelsrød's circulations cannot grow to detectable levels, and it is very likely that Coriolis accelerations may be neglected altogether when considering the growth of Langmuir circulations of all previously reported length scales (although the effect of an established Ekman layer presumably may modify the motion in larger

† Part 1 of this paper (Leibovich 1976) had already been prepared before these papers appeared and therefore they were not discussed there.

scale Langmuir circulations, the Coriolis acceleration itself should be otherwise negligible in all respects in their formation).

Garrett's mechanism is a complicated instability, and is based upon the following ideas. An initial spanwise perturbation with speed $U(y)$ is taken in water of infinite depth, where y is a horizontal co-ordinate perpendicular to the direction of U. This perturbation is assumed to be independent of the wind direction x, and variations of U with respect to the vertical co-ordinate z are assumed to be ignorable. Surface waves travelling at an angle to the wind are refracted by the current, leading to an increase in the wave energy on the line of maximum U. This set of events produces an average force that creates a mean-flow convergence towards the line of maximum U, and increased wave breaking along this line reinforces U.

Questions can be raised concerning the applicability of the Garrett model to Langmuir circulations (as, indeed, may be done with the present model as discussed below). The points we find most troublesome are the following. (1) The model deviates from the understood usage of wave–mean-flow interaction analyses without comment. By averaging the equations of motion for the fluid above a certain depth h (below the mean free surface), as described by Phillips (1966), the waves are seen to exert a force on the mean flow. It is then assumed that, in some undescribed fashion, the force exerted by the waves on the mean flow of water above depth h, which in the usual theory of wave–mean-flow interaction is distributed through the water depth, is transmitted as a stress on the water below depth h. As far as we can tell, there is no mechanical basis for this step. There is no clear way to determine h; one can increase h by any multiple as far as the usual wave–mean-flow interaction methods are concerned; as a matter of fact, in such theories h is taken as the total water depth. One would normally believe that, as the theory of wave–mean-flow interactions contemplates, the forces exerted by the waves on the mean flow are balanced primarily by accelerations of the mean flow above depth h. (2) The neglect of a vertical variation of U cannot be justified. (3) The stress exerted by the wind is not explicitly required. In particular, it would seem that Langmuir-circulation 'windrows' should sometimes form, if the Garrett mechanism is appropriate, in the absence of wind. This does not seem to occur.

The physical basis of the Craik–Leibovich theory is succinctly described in the introduction to part 1 of this paper (Leibovich 1976). In brief, vorticity in the sheared current created by the wind stress is distorted by spanwise-variable Stokes drift, creating a component of vorticity in the wind direction. The circulations generated in this way are therefore directly driven by the wind drift current and its interaction with surface waves. For the surface waves to produce the spanwise-variable Stokes drift, a degree of regularity of the wave spectrum is required that may be unrealistic in practice and this may be a serious objection to the present theory. In particular, the surface waves need to be phase locked for many (perhaps 100) wave periods. The point is discussed at greater length in §6. A. D. D. Craik (1977) has pointed out, however, that the mathematical model developed in CL, as generalized in part 1, allows circulations to be generated by means of a Stokes-drift-driven instability almost completely analogous to thermal convection. The Stokes drift required need not have spanwise variations and a random wave field can be assumed.

In part 1 the CL theory was extended to remove the basically limiting assumption of quasi-steady flow and the improved theory was used to discuss the horizontally averaged wind drift current. In the present paper, a numerical method free from

difficulties encountered in CL is used to calculate the detailed current system using the equations developed in part 1. The results pertaining to the horizontally averaged current that is one component of the interconnected system of wind drift currents and Langmuir circulations have already been presented in part 1. The object of this paper is to describe the computations, and to examine the relationships between the results and the five features listed above. The focus here is therefore on the vertical motions and on the detailed structure of the Langmuir cells. All five features are reproduced by the solutions described in this paper. Some specific quantitative features of the current pattern which should be amenable to experimental test are the following:

(i) the maximum horizontal sweeping speed (velocity component towards convergence zones) at the surface is very close to the maximum downwelling speed,

(ii) if L is the distance between upwelling and downwelling zones (half the distance between streaks) the surface sweep referred to in (i) reaches its maximum at a position that is about $0{\cdot}25L$ to $0{\cdot}3L$ from the convergence zones,

(iii) the downwelling speeds are typically more than twice the upwelling speeds,

(iv) the system of wind drift currents and Langmuir circulations near the surface is established after a time period of about $10T_d$, where

$$T_d = \sigma^{-1}(\nu_T \sigma)^{\frac{1}{2}}/\epsilon u_*,$$

σ is a typical wave angular frequency, ϵ is a measure of wave slope, u_* is the water friction velocity and ν_T is an eddy viscosity. It is shown in part 1 that T_d is of the order of minutes in typical cases. After this period of growth, the near-surface current system is essentially invariant although the mathematical problem as a whole has no steady limit.

Additional statements can be made by using known results (not related to Langmuir circulations) about the surface drift current, and often-used correlations about wind waves, to relate the eddy viscosity to the sea state and wind speed. These results can be found in §5.2. Although this procedure is speculative, it leads to a simple relation (equation (25)) linking the current system to the wind speed and sea state. Furthermore, (25) seems to yield quantitatively realistic results for all three components of the system of currents and circulations.

Detailed velocity measurements have not been made in Langmuir circulations, and a systematic series of current measurements poses an extremely difficult experimental task. Yet until such measurements are made no theoretical mechanism of the Langmuir circulations can be satisfactorily verified. Nevertheless, despite the doubt that exists about the underlying assumptions concerning the surface wave field, (25) seems to predict what *is* known about the current structure sufficiently well to be used now as a mathematic model for the mixing accomplished by Langmuir cells.

The instability mechanism suggested by Craik requires a minimum of *a priori* assumptions, and therefore offers very attractive possibilities as a theoretical explanation of Langmuir circulations. The details need to be explored, and the theoretical predictions, particularly of finite-amplitude convective motions, must be compared with observation. One might expect, however, that the instability mechanism would lead to finite-amplitude motions that are similar to the results of the present calculations. Both the present mechanism and the instability mechanism are based upon the same set of rectified equations (those presented in part 1), and consequently follow from the same scalings and ordering assumptions. It is also possible that the direct

coupling of wind and waves inherent in the present model may provide initial perturbations that then continue to grow by the instability mechanism. To perform this function, the waves need be phase-locked only for a relatively short time.

2. The model problem for the evolution of the current system

The model of part 1 treats a body of constant-density water of infinite depth. For time $t < 0$, the water is at rest in $z \leqslant 0$, while for $t \geqslant 0$ a constant shear stress in the x direction due to the wind is imposed at the mean free surface $z = 0$. Let $\mathbf{i}$, $\mathbf{j}$ and $\mathbf{k}$ be unit vectors in the x (wind), y and z (vertical) directions, and let the co-ordinate system be right-handed. A surface wave field is assumed to exist, and to have wave parameters (frequency, wavenumber vectors, amplitude spectrum) that are fixed in time. In particular, the following wave model is specifically treated in part 1 and in the present paper:

$$\mathbf{u}_w = \text{grad}\,(2a\sigma\kappa^{-1} e^{\kappa z} \cos(\kappa y \sin\theta) \cos(\kappa x \cos\theta - \sigma t)), \tag{1}$$

where $\mathbf{u}_w$ is the velocity produced by the wave motion alone. The velocity field (1) arises from the superposition of a small-amplitude irrotational wave train of frequency σ, wavenumber vector

$$\boldsymbol{\kappa} = \kappa(\cos\theta\mathbf{i} + \sin\theta\mathbf{j}), \tag{2}$$

and amplitude a, and a second wave train that differs only by the replacement of θ by $-\theta$ in (2). Since $\mathbf{i}$ is a unit vector in the wind (x) direction, and $\mathbf{j}$ is a unit vector in the y direction, the motion in (1) is the simplest representation of a short-crested wave field, with directional characteristics symmetric with respect to the wind direction. If the complete equations are averaged over a number of wave periods as described in part 1, the waves produce a driving force in the equations for the developing current system. The currents then develop in response to the wave-induced driving force and to the wind stress imposed on $z = 0$

$$\tau_w = \rho u_*^2,$$

where u_* is a water friction velocity. It is shown in part 1 that if the current (the non-oscillatory part of the water motion) is scaled in the following way,

$$\mathbf{U}_c = (u_*^2/\nu_T\kappa)\, u\mathbf{i} + (u_* a/\nu_T)(\sigma\nu_T)^{\frac{1}{2}}(V\mathbf{j} + W\mathbf{k}), \tag{3}$$

where ν_T is an eddy viscosity that is assumed to be constant, and if lengths are scaled by κ^{-1} and time by

$$(a\kappa u_*)^{-1}(\nu_T/\sigma)^{\frac{1}{2}}, \tag{4}$$

then the development of the current system is described by the equations

$$u_t + Vu_y + Wu_z = La\nabla^2 u, \tag{5a}$$

$$\Omega_t + V\Omega_y + W\Omega_z = La\nabla^2\Omega + F, \tag{5b}$$

$$F \equiv \partial(u_s, u)/\partial(y, z), \tag{5c}$$

$$u_s \equiv 2\cos\theta e^{2z}[1 + \cos^2\theta\cos(2y\sin\theta)], \tag{5d}$$

$$\nabla^2\Psi = -\Omega, \quad \nabla^2 = \partial^2/\partial y^2 + \partial^2/\partial z^2, \tag{5e}$$

$$V = \Psi_z, \quad W = -\Psi_y, \tag{5f}$$

$$La \equiv (\nu_T\kappa/au_*)(\nu_T/\sigma)^{\frac{1}{2}}. \tag{5g}$$

The wave forcing is felt through u_s, which is a Stokes-like wave drift that acts to stretch vortex lines in the current. The problem (5*a–g*) depends upon the two parameters θ and La, the latter being called the 'Langmuir number' in part 1.

A solution of (5) with the same y periodicity that appears in u_s is possible, and we may calculate this solution by imposing the boundary conditions

$$\Psi(0,z,t) = \Psi(L,z,t) = 0, \tag{6a}$$

$$\Omega(0,z,t) = \Omega(L,z,t) = 0, \tag{6b}$$

$$\frac{\partial u}{\partial y}(0,z,t) = \frac{\partial u}{\partial y}(L,z,t) = 0, \tag{6c}$$

where

$$L = \pi/2\sin\theta. \tag{6d}$$

The two planes $y = 0, L$ define a cell that comprises half of the y period of a motion that is assumed to take place in $|y| \leqslant \infty, z \leqslant 0$. A constant shear stress in the wind direction is assumed to be the only component of the applied stress vector that acts upon the surface $z = 0$. The scalings used in (5) are chosen so that the applied stress condition may be written

$$\frac{\partial u}{\partial z}(y,0,t) = 1. \tag{7a}$$

The plane $z = 0$ is also a stream surface for the current, so we must have

$$\Psi(y,0,t) = 0 \tag{7b}$$

and (7*b*) may be used to write the required condition on the y component of the applied surface stress as

$$\Psi_{zz}(y,0,t) = 0. \tag{7c}$$

Conditions (7*b*) and (7*c*) imply that

$$\Omega(y,0,t) = 0 \tag{8}$$

and, as $z \to \infty$ for $t < \infty$, we impose the conditions

$$u, \Psi \to 0. \tag{9}$$

The initial conditions are

$$u(y,z,0) = \Psi(y,z,0) = 0. \tag{10}$$

Equations (5) and conditions (6–10) constitute the complete mathematical statement of the problem that we consider in this paper.

If (5*a*), written in divergence form, is integrated over a cell ($-\infty < z \leqslant 0, 0 \leqslant y \leqslant L$) and the stress condition (7*a*) is applied, one sees that the x momentum of the fluid in the cell increases with time according to $Lt(La)$. As in part 1, we define the horizontally averaged x velocity component to be

$$\bar{u} = \frac{1}{L}\int_0^L u(y,z,t)\,dy. \tag{11}$$

Let M be the x momentum per unit width of cell, then

$$M(t) = \int_{-\infty}^{0} \bar{u}\,dz = tLa. \tag{12}$$

The result (12) will be referred to in subsequent discussions.

3. The finite difference approximation

This section contains a description of the numerical methods employed in this research. The description is organized in four subsections: §3.1 deals with the finite difference representations of equations (4), §3.2 describes the treatment of boundary conditions, §3.3 describes the sequencing involved in the advancement of the solution by one time step and §3.4 describes the checks of accuracy, convergence and the conservation of momentum.

3.1. *Finite difference representations*

The flow region corresponding to a single cell was covered by a rectangular set of points. The y interval $0 \leqslant y \leqslant L$ was covered by a mesh $y_i = (i-1)\Delta y$, $i = 1, 2, \ldots, NY$. Typically, the mesh included 21 points, plus two dummy points used to satisfy conditions at the y boundaries; although some calculations were also carried out with 11 and 41 points. The infinite interval $z \leqslant 0$ was represented by a uniform mesh that at a given instant contained the $NZ+1$ points $z_j = -(j-1)\Delta z$, $j = 1, 2, \ldots, NZ+1$. The total number of z mesh points was increased as time progressed; the number NZ at any given level of time was determined internally in the program in a manner to be described in §3.2. Typical mesh sizes for Δz included 0·02, 0·05, 0·1 and 0·12. All mesh sizes yielded qualitatively similar results, and the Δz for a particular run was usually chosen as a compromise between accuracy and economy.

The numerical method used was a standard explicit two-time-level algorithm. Time derivatives were represented by forward time differences, and the x momentum and vorticity equations (5*a*, *b*) were approximated by conservative finite-difference equations. Convective derivatives in conservation form were approximated by the second-upwind difference method (see Roache 1972, p. 73). All Laplacian operators in (5) were replaced by five-point difference formulae. The vorticity generation term F was evaluated by analytically differentiating u_s as needed [see 5(*c*, *d*)], and by using centred-difference formulae for u_y and u_z. The stream function was found from the finite difference analogue of the Poisson equation (5*e*) by the method of successive over-relaxation, using the optimum relaxation factor for rectangular domains.

3.2. *Boundary conditions*

The boundary condition $u \to 0$ as $z \to -\infty$ was replaced by the condition that the ratio of the maximum value of u on the $j = NZ$ row of points to the maximum value of u at the surface ($j = 1$) be less than 10^{-5}. Since the scheme is explicit, this condition is convenient to apply. Each advancement of time from a level $n\Delta t$ to $(n+1)\Delta t$ causes a change of u (and Ω) on the $j = NZ$ row (both u and Ω are set to zero on $j = NZ+1$). When u exceeded the specified limit on this line, NZ was increased by one and the solution repeated until NZ was large enough to allow the condition on u to be met. We refer to the depth $z = -NZ\Delta z$ as the 'depth of influence', since it marks the perceptible depth of penetration of momentum. The remaining equations are then solved with the enlarged net, and the depth of influence is verified by ensuring that the vorticity Ω at the depth of influence is less than 10^{-4}. If it is larger than this value, the depth of influence is increased and the solution repeated. The net thus grows in size as time

increases in a way that naturally reflects the penetration of flow disturbances with time.

The exact boundary conditions require the vorticity Ω to vanish at all boundary points for all values of time. The Ω and F fields are therefore initialized at zero, and are evaluated only at internal grid points. Similar remarks apply to the stream function Ψ. It was found, however, that the application of the condition $\Psi = 0$ at the lower boundary led to z gradients in Ψ (i.e. v velocity components) sufficiently large to indicate that a condition approximating $\Psi = 0$ had not been achieved. The reason for this situation is clear: the lower boundary is set to be the 'depth of influence', which is a measure of the penetration distance of the vorticity. The stream function decays exponentially fast below a depth measured from the region of significant vorticity accumulation. Thus its decay effectively begins at a level shifted down from the surface, and the decay is not yet sufficiently great at the depth of influence to have both Ψ and Ψ_z negligibly small. In order to improve accuracy, a modified boundary condition (suggested by the outer solution (34) of part 1),

$$\Psi_z = 2\sin\theta\Psi, \tag{13a}$$

at the lower boundary was used. Since $z = -NZ\Delta z$ at the depth of influence, the implementation of this boundary condition by use of backward differences produces the relation

$$\Psi_{i,NZ+1} = \Psi_{i,NZ}/(1+2\sin\theta\Delta z), \tag{13b}$$

which was used as the lower boundary condition for Ψ. Experiments on the model problem

$$\nabla^2\Psi = -e^z\sin y, \quad \Psi(y,0) = \Psi(0,z) = \Psi(\pi,z) = 0, \quad \Psi\to\infty \quad \text{as} \quad z\to-\infty$$

using both the boundary condition (13b) and $\Psi = 0$ at the lower boundary proved (13b) to be much superior. The model problem, a good simulation of the physical problem, has the exact solution $\Psi = -\frac{1}{2}ze^z\sin y$. As an example, the depth of influence was set at 4 and the finite difference solution to the model problem was obtained using (13b) with $\Delta y = \frac{1}{10}\pi$ and $\Delta z = 0{\cdot}2$. The numerical solution at $z = -4$ and $y = \frac{1}{2}\pi$ was $\Psi = 0{\cdot}0330$, which may be compared with the exact solution $\Psi = 0{\cdot}0367$ at that point. The straightforward boundary condition would, of course, yield $\Psi = 0$ at the point in question.

The method of satisfying the lower boundary condition for u has been outlined in our discussion of the definition of the depth of influence. The boundary conditions on u at the top and the sides are of Neumann form: on the sides $\partial u/\partial y = 0$ and on the top $\partial u/\partial z = 1$. These conditions were handled by the use of dummy points, and by solving special forms of (5a) along the boundary lines. At the left end of the cell ($i = 1$), the condition $\partial u/\partial y = 0$ is satisfied by taking $u_{2,j} = u_{0,j}$ where $i = 0$ represents the column of image points that is the reflexion in $i = 1$ of the column $i = 2$. (The notation is $u_{i,j} = u(y_i, z_j)$, where $y_i = (i-1)\Delta y, z_j = -(j-1)\Delta z$.) This condition, together with the observation that v is an odd function of y, leads to a special form of the finite difference analogue of (5a) that is applicable on the $i = 1$ column. Similar remarks apply to the right-hand side of the cell $y = L$.

The boundary condition (7*a*) is to be simulated at the top ($y = 0, j = 1$) of the mesh, and this is also treated by a dummy row of points $j = 0$, and by the use of a special form of (5*a*) to describe the evolution of u along $y = 0$. Since $w = 0$ at $y = 0$, the differential equation for u can be written

$$\partial u/\partial t = -v\,\partial u/\partial y + La\nabla^2 u.$$

Making use of the dummy points, this equation is represented by the finite difference analogue

$$\frac{u_{i,j}^{n+1} - u_{i,j}^{n}}{\Delta t} = -v_{i,1}^{n}\,\frac{u_{i+1,j}^{n} - u_{i-1,j}^{n}}{2\Delta y} + La\left\{\frac{u_{i+1,1}^{n} - 2u_{i,1}^{n} + u_{i-1,1}^{n}}{(\Delta y)^2} + \frac{u_{i,2}^{n} - 2u_{i,1}^{n} + u_{i,0}^{n}}{(\Delta z)^2}\right\}. \quad (14a)$$

Values of u along the dummy row are replaced in (14*a*) by the finite difference representation of the stress boundary condition

$$(u_{i,0}^{n} - u_{i,2}^{n})/2\Delta z = 1$$

or

$$u_{i,0}^{n} = u_{i,2}^{n} + 2\Delta z. \quad (14b)$$

Although the finite difference equations are written in conservation form, the boundary condition (14*a*, *b*) is not conservative, and the overall scheme therefore is not in conservation form. Our earlier numerical experiments indicated that the method described was more accurate, when compared with analytical solutions valid for small time, than a fully conservative treatment. The present method was therefore used, and momentum was numerically computed to assure that unacceptable momentum sources or sinks did not appear (cf. §3.4).

3.3. *Description of a computational cycle*

The sequence for advancement of the solution from time t_n to the new level

$$t_{n+1} = t_n + \Delta t$$

is as follows:

(1) The speed u in the wind direction is advanced at all grid points with the difference approximations and boundary conditions discussed in §§3.1 and 3.2. The depth of influence is checked and if necessary a new depth is generated.

(2) The forcing function F is calculated at all interior grid points as described above, using values of u at the new time level.

(3) The vorticity Ω at all interior grid points is then advanced.

(4) The depth of influence is verified by applying the test described in §3.1 on the vorticity. If necessary the depth is increased and steps 1 to 3 are repeated on the grid points in the additional row.

(5) The stream function Ψ is advanced at all grid points with the boundary condition (13*b*) used on the lower boundary.

(6) The velocities v and w are determined from the new stream-function field.

(7) The average velocity $\bar{u}$ and Reynolds stress $-\overline{uw}$ (presented in part) are computed at each row using Simpson's rule. The momentum $M(t)$ (equation (12)) is evaluated from $\bar{u}$ by the trapezoidal rule

(8) The field of mesh points is scanned in order to ensure that the time step Δt is not greater than the stable time step. This stability requirement is discussed in the next subsection.

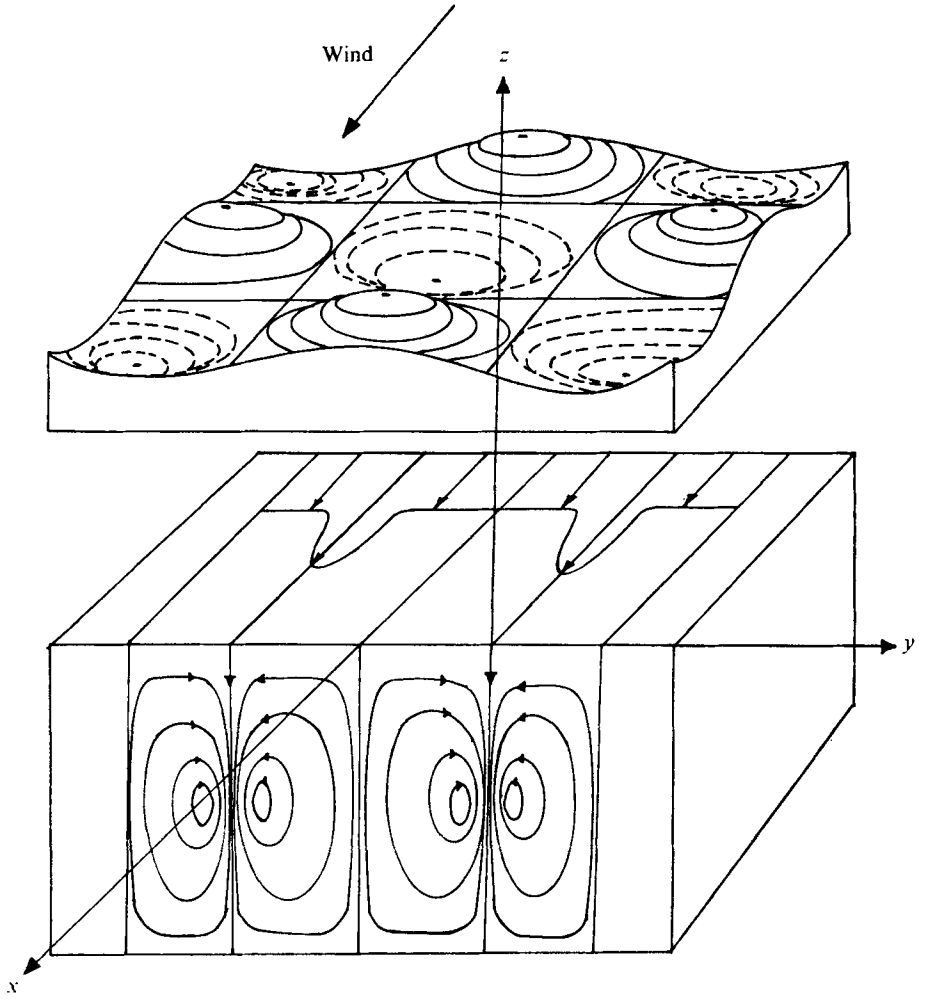

FIGURE 1. Sketch of the predicted motions, showing the relationship between the surface wave field, the surface wind-directed drift current (Stokes drift excluded), and the subsurface convective motions.

As an example of the variation of the computational parameters, the number of grid points in the mesh increased from 1407 at $t = 5$ to 6615 at $t = 35$ for $\theta = 30°$, $La = 0{\cdot}01$, $\Delta y = 0{\cdot}157$, $\Delta z = 0{\cdot}02$. The number of computational cycles required to advance the solution by unit time was typically 100.

3.4. *Checks on the numerical solution*

The following checks were made to support the numerical solution.

(1) Stability of the scheme is achieved by restricting the time step Δt; no restrictions are imposed on the spatial mesh. The schemes used in the solution for u and Ω require that

$$\Delta t \leqslant \left[2La\left\{\frac{1}{(\Delta y)^2}+\frac{1}{(\Delta z)^2}\right\}+\frac{V_{i,j}+V_{i+1,j}}{2\Delta y}+\frac{W_{i,j}+W_{i,j+1}}{2\Delta z}\right]^{-1}.$$

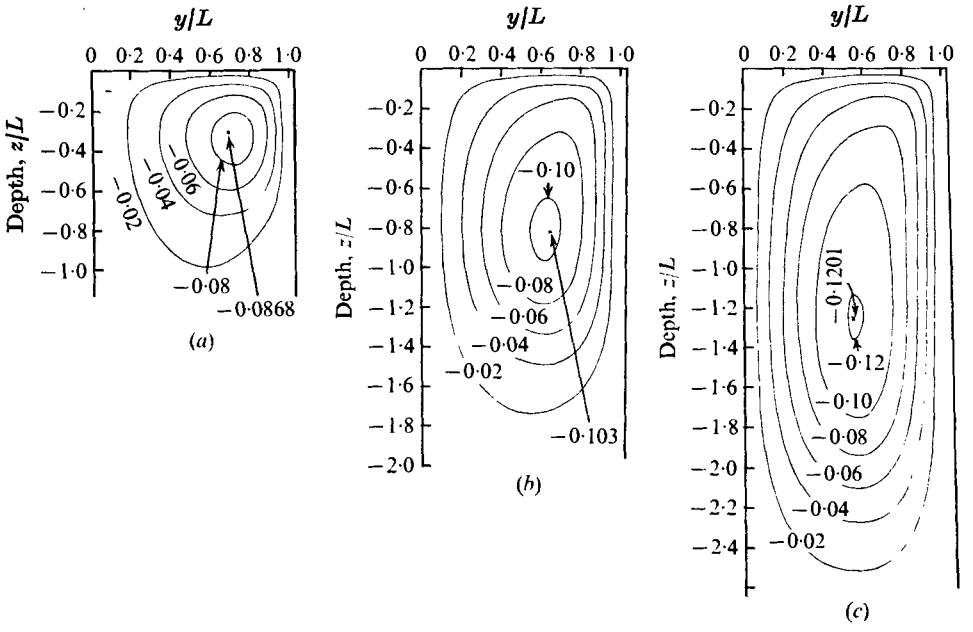

FIGURE 2. Streamlines in the plane perpendicular to the wind for $\theta = 30°$ and $La = 0{\cdot}01$, for various dimensionless times. (*a*) $t = 16$, (*b*) $t = 31$, (*c*) $t = 63$.

The field of mesh points was scanned in order to determine the largest allowable Δt that will satisfy the stability requirements. In our computational runs a constant value of Δt was used and comparisons were made to ensure that this did not exceed the stable value of Δt.

(2) The accuracy of the solution at small time was assessed by comparing the solution for u with the exact solution of the Rayleigh problem, and with the small time extension derived in part 1. For times up to $t = 2$, the error was less than a fraction of a per cent for the finest mesh used.

(3) The conservation of momentum provides a precise global check on the solution for all time t and was continually monitored as the solution unfolded. The maximum error in global momentum in the numerical solution with $\Delta z = 0{\cdot}02$ is around $0{\cdot}2\,\%$; with $\Delta z = 0{\cdot}1$, it did not exceed $7\,\%$.

4. Computed motions in a cell

In order to place the figures to follow in proper orientation with respect to the surface wave field we point out that $y = 0$ corresponds to a line along which peaks of the wave field (1) propagate, and $y = L$ is a nodal line with zero displacement of the mean free surface. Therefore, the wave drift u_s is greatest on the line $y = 0$ and least at $y = L$. The sketch in figure 1 may be of help in picturing the situation.

Figure 2 illustrates the evolution of the streamline pattern computed for a Langmuir cell for $\theta = 30°$ and $La = 0{\cdot}01$. For very early time levels (not shown) the vortex centre is on the line $y = \frac{1}{2}L$, and the motion is symmetric. An interesting feature, however, is the development of a strong asymmetry that is manifest at $t = 10$. Downwelling is significantly stronger than upwelling motions at $t = 10$, and the horizontal motions

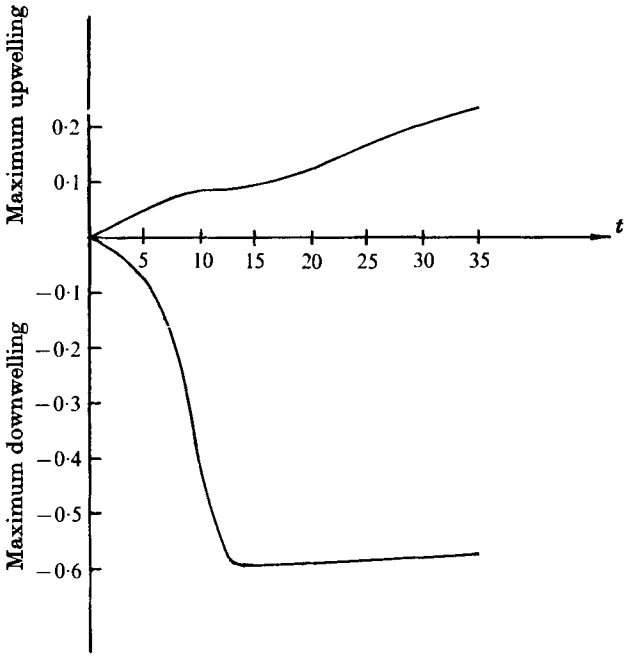

FIGURE 3. Maximum vertical speeds on the planes of convergence (downwelling) and divergence (upwelling) as a function of dimensionless time for $\theta = 30°$ and $La = 0{\cdot}01$. Notice the difference between the magnitudes of upwelling and downwelling speeds. Downwelling speeds have a clearly defined characteristic development time, and change slowly for larger times.

are strongest at the surface. As an illustration of the asymmetry, upwelling and downwelling speeds on lines of convergence ($y = L$) and divergence ($y = 0$) are plotted in figure 3 as a function of time for $\theta = 30°$. The greatest difference in upwelling and downwelling speeds occurs between $t = 10$ and $t = 15$.

This asymmetry relaxes somewhat at later times, although it is still a distinct feature at the largest values of time that we have computed. If we follow the vortex centre in time, it moves to the right and downward, and then reverses its horizontal movement and creeps back towards the horizontal centre of the cell while continuing its slow descent into the fluid below. The time of reversal of the vortex-centre movement is reflected in changes in the time behaviour of other features of the solution. Upwelling and downwelling have already been mentioned. Another example is the time behaviour of the maximum and minimum values of the u velocity component at the surface, which is shown in figure 4.

The explanation for these overshoots is thought to be as follows: the time period between the initiation of motion and the reversal of the vortex-centre motion corresponds to the time period required to establish the equilibrium structure in the $\bar{u}$ currents that is described in part 1. Gradients of $\bar{u}$ are greatest in this time period. These gradients subsequently are smoothed by the mixing that is developed in the circulations until an 'equilibrium' is established, after which $\bar{u}$ changes very slowly and maintains its basic structure. This initial starting-up period is therefore one in which the rate of growth of vorticity is greatest. The developing convection serves to transport vorticity vertically downward and therefore smooths out a vorticity buildup.

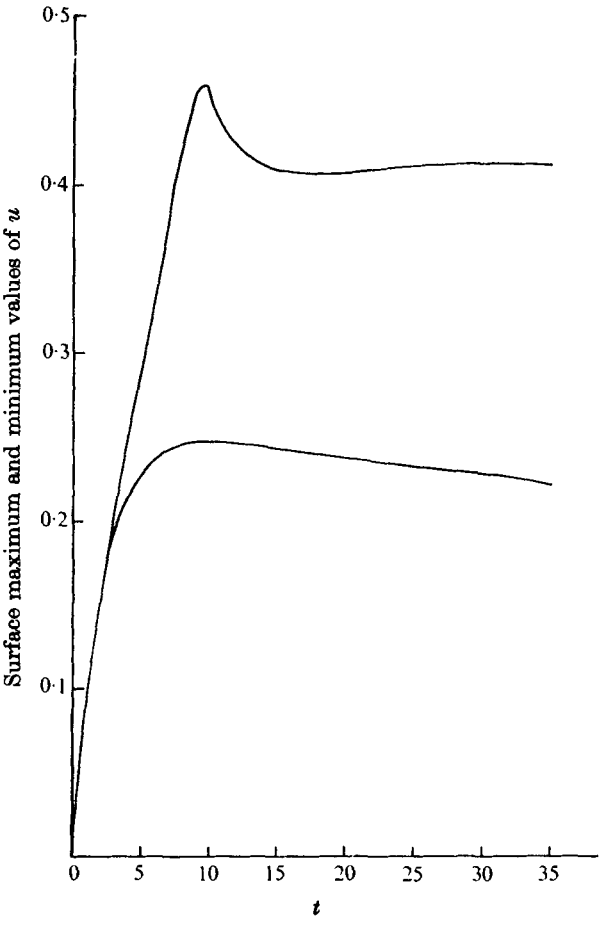

FIGURE 4. Maximum and minimum values of the x velocity component at the surface as a function of time for $La = 0{\cdot}01$ and $\theta = 30°$.

The history of streamline patterns for the case $\theta = 15°$, $La = 0{\cdot}01$ is much the same as the $\theta = 30°$ example, and is shown in figure 5. A longer time is required for the development of the motion. The cell is almost twice as wide as the $\theta = 30°$ cell, but the velocities that develop are comparable. Consequently, the convection time for $\theta = 15°$ is nearly double the convection time for $\theta = 30°$, and the time required to establish (geometrically) similar stages of motion is therefore nearly twice as long for $\theta = 15°$ as it is for $\theta = 30°$. Of course, since the velocity fields are comparable, actual rates of penetration of the depth of influence are also comparable.

Figures 6 and 7 present contour lines for x vorticity for $\theta = 30°$ and 15°. The region of vorticity generation near the surface is clear. At greater depths, vorticity changes occur owing to convection and diffusion only, and the former is dominant. Thus, the vorticity contour lines are essentially material lines, and the changes as time increases can be interpreted reasonably well from this viewpoint. Two expanded views of the region of vorticity generation near the surface are given in figure 8 for both angles θ. These patterns remain essentially independent of time for each angle in these regions, which correspond to the 'equilibrium' regions discussed in part 1.

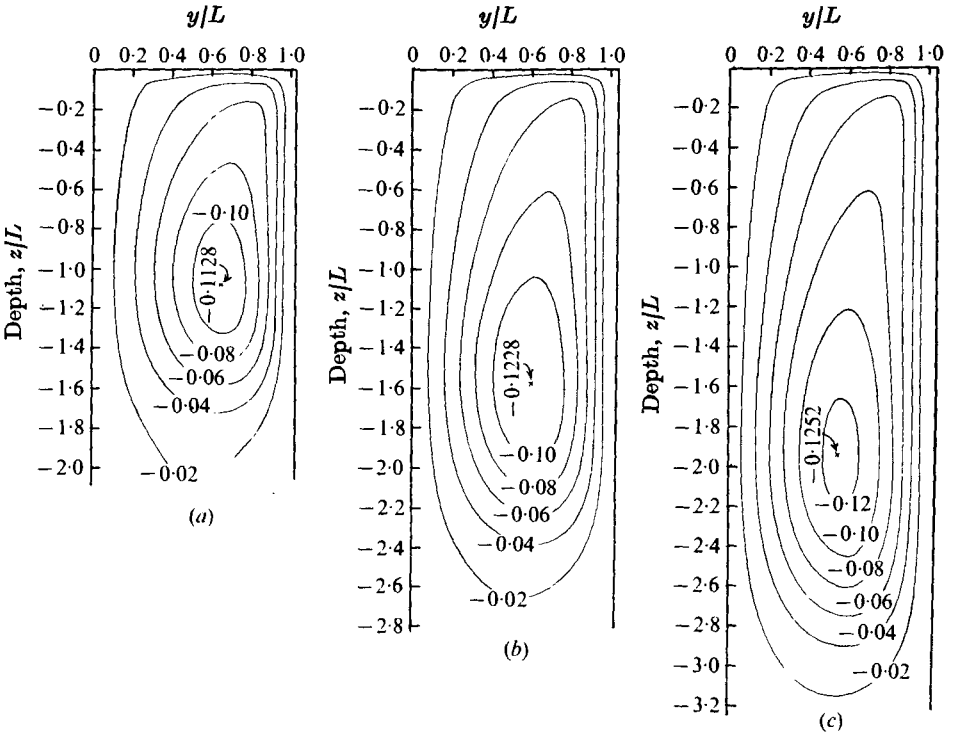

FIGURE 5. Streamlines in the plane perpendicular to the wind for $\theta = 15°$ and $La = 0{\cdot}01$, for various dimensionless times. Streamlines for $t = 30$ have been presented in part 1 of the paper. (*a*) $t = 61$, (*b*) $t = 91$, (*c*) $t = 121$.

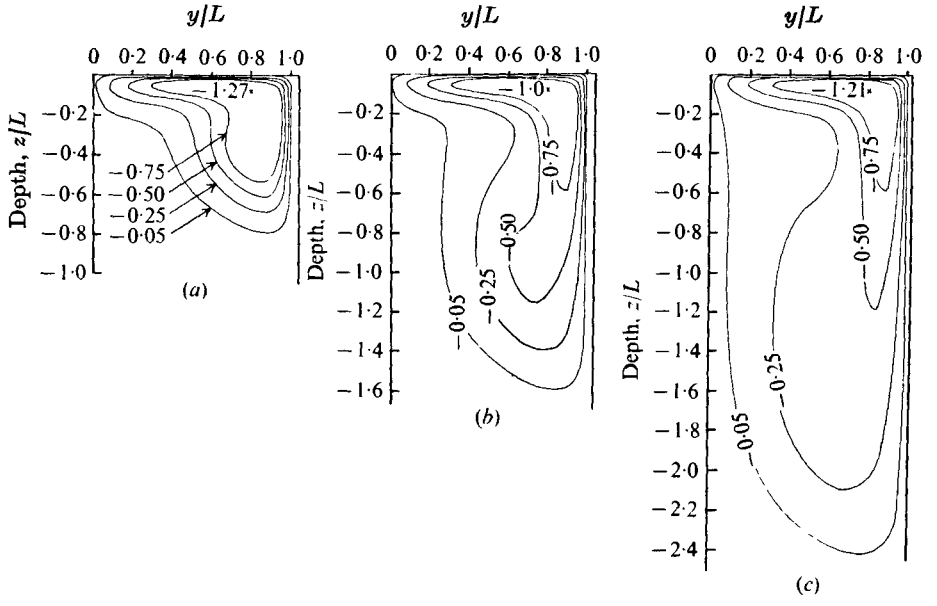

FIGURE 6. Contour lines for the x component of vorticity Ω for $\theta = 30°$, $La = 0{\cdot}01$, for various times. (*a*) $t = 15$, (*b*) $t = 31$, (*c*) $t = 63$.

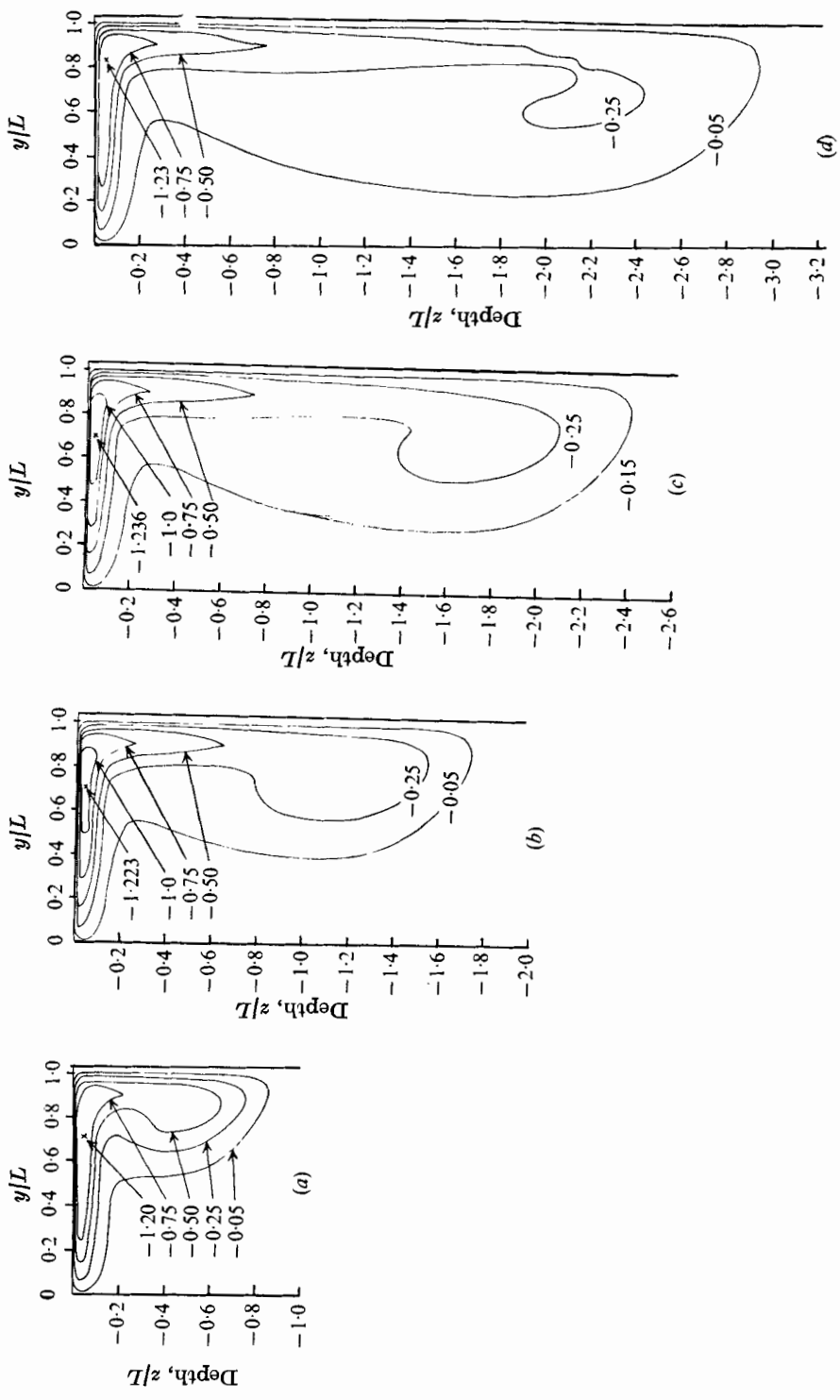

FIGURE 7. Contour lines for the x component of vorticity Ω for $\theta = 15°$, $La = 0{\cdot}01$, for various times.
(*a*) $t = 30$, (*b*) $t = 61$, (*c*) $t = 91$, (*d*) $t = 121$.

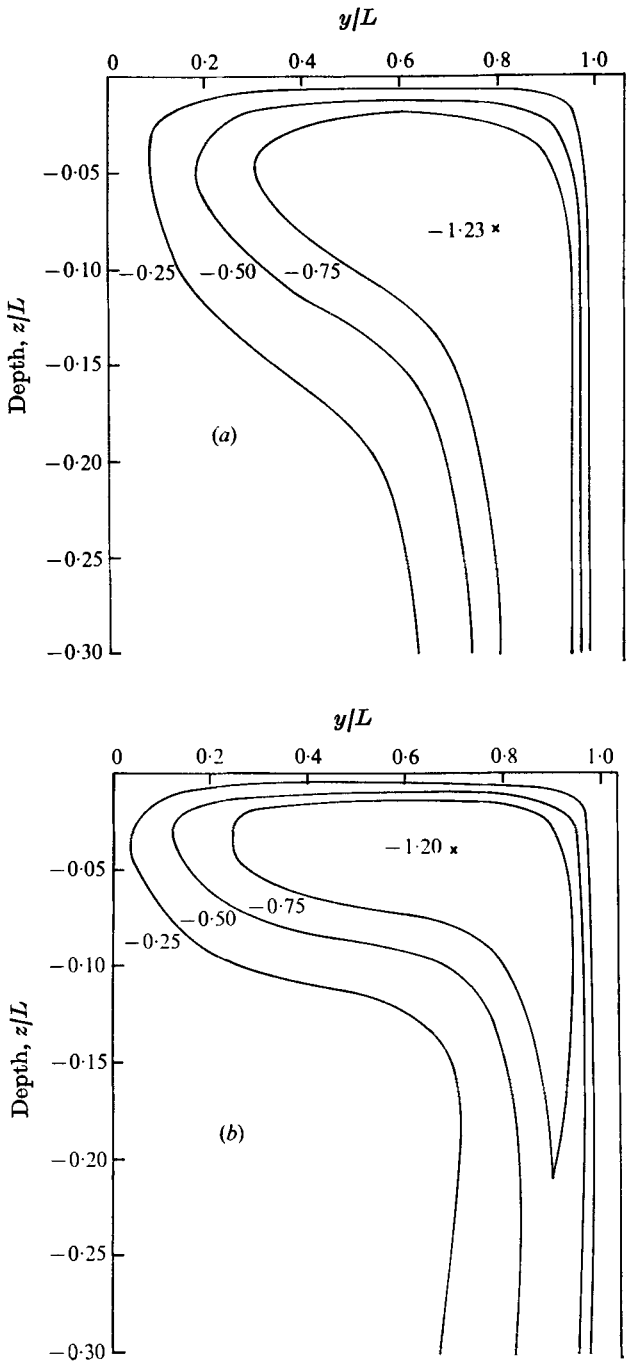

FIGURE 8. Contour lines for vorticity component Ω, in the fluid near the surface. (*a*) $\theta = 30°$, $t = 31$, $La = 0{\cdot}01$, (*b*) $\theta = 15°$, $t = 30$, $La = 0{\cdot}01$.

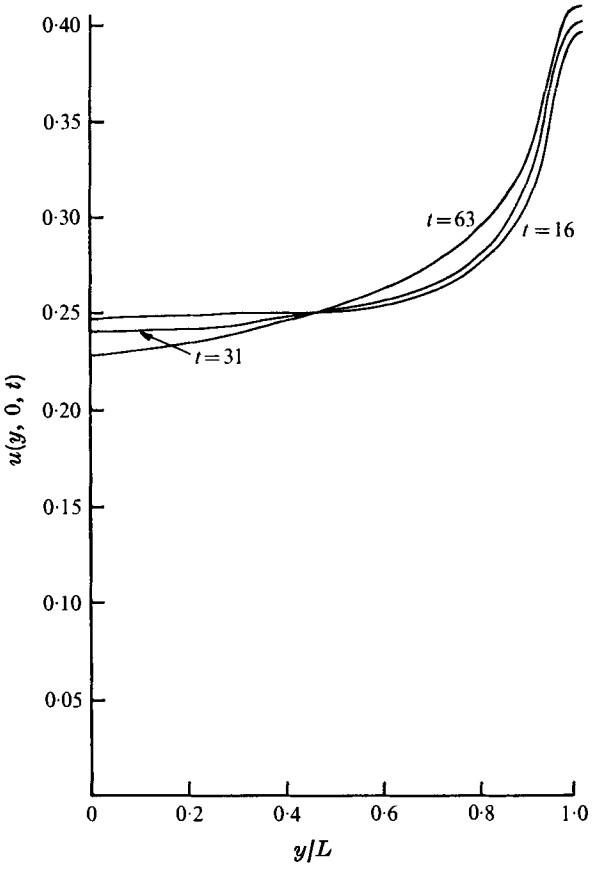

FIGURE 9. The wind-directed current speeds at the surface as a function of the spanwise co-ordinate y for $\theta = 30°$, $La = 0{\cdot}01$.

The wind-directed surface current speeds for $\theta = 30°$ at various times are shown in figure 9 as a function of the spanwise co-ordinate y. The corresponding information for $\theta = 15°$ is given in figure 10. At all time levels shown in these figures, a sharp peak in $u(y, 0, t)$ occurs over convergence planes ($y = L$), and the profile is flat over the remaining portion of the surface. Peak speeds exceed minimum speeds by more than 60 % for $\theta = 30°$ and by more than 50 % for $\theta = 15°$. The existence of a local maximum in the surface wind-directed current located over downwelling zones is essential to obtain the fourth of the features listed in § 1. The issue is somewhat confused, however, by the concurrent action of the Stokes mass transport, and we shall return to this question in the next section. The evolution of the subsurface behaviour of u is shown in velocity profiles taken through slices of the cell at the planes $y = 0$, $y = \frac{1}{2}L$, and $y = L$ for $\theta = 30°$ in figure 11. The corresponding figure for $\theta = 15°$ has already been presented in part 1.

Vertical velocities are plotted as functions of depth at the planes of convergence and divergence in figures 12 and 13 for $\theta = 30°$ and 15°, for various times. These figures provide more detail on upwelling and downwelling motions than is given in figure 3. Notice that the maximum downwelling occurs (in each figure) at approximately the

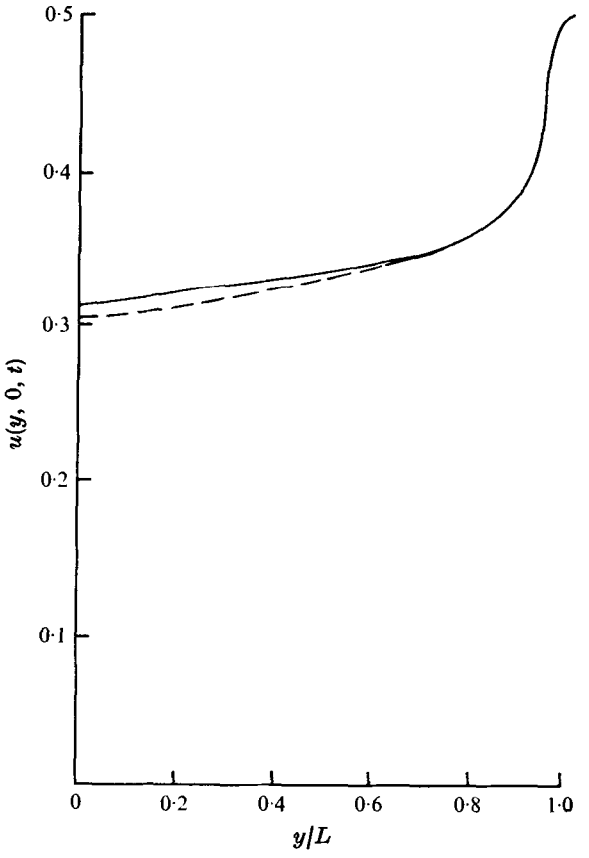

FIGURE 10. The wind-directed current speeds at the surface as a function of the spanwise co-ordinate y for $\theta = 15°$, $La = 0{\cdot}01$. —, $t = 30$; – – –, $t = 61, 91, 121$.

same depth for all times shown, but that the maximum upwelling speeds seem always to occur at about one half of the depth of influence. Thus, the largest upwelling speeds occur at progressively greater depths. The maximum downwelling speeds change very little with time after the velocity overshoots subside. The numerical values for the maximum downwelling are about 50 % greater than the maximum surface value of u. This does not imply, however, that the physical maximum downwelling speeds predicted by the model necessarily exceed the maximum surface value of the x velocity component; as equation (3) shows, the scaling for these components differs by a constant factor. Maximum upwelling speeds on the divergence plane $y = 0$ grow slowly with time. Only for largest values of time shown does the upwelling exceed half of the maximum downwelling.

The surface value of the spanwise velocity component $V(y, 0, t)$ is shown in figures 14 and 15 for $\theta = 30°$ and $\theta = 15°$. This is the component of velocity that sweeps surface material into rows above the convergence plane. In both figures 14 and 15, the curves for $V(y, 0, t)$ for $t = 60$ and 90 essentially coincide, so only one curve is drawn for both time levels. By comparing values given in these figures with those in figures 12 and 13 (V and W have the same dimensional scaling) one sees that the maximum horizontal sweeping velocities slightly exceed the maximum downwelling speeds.

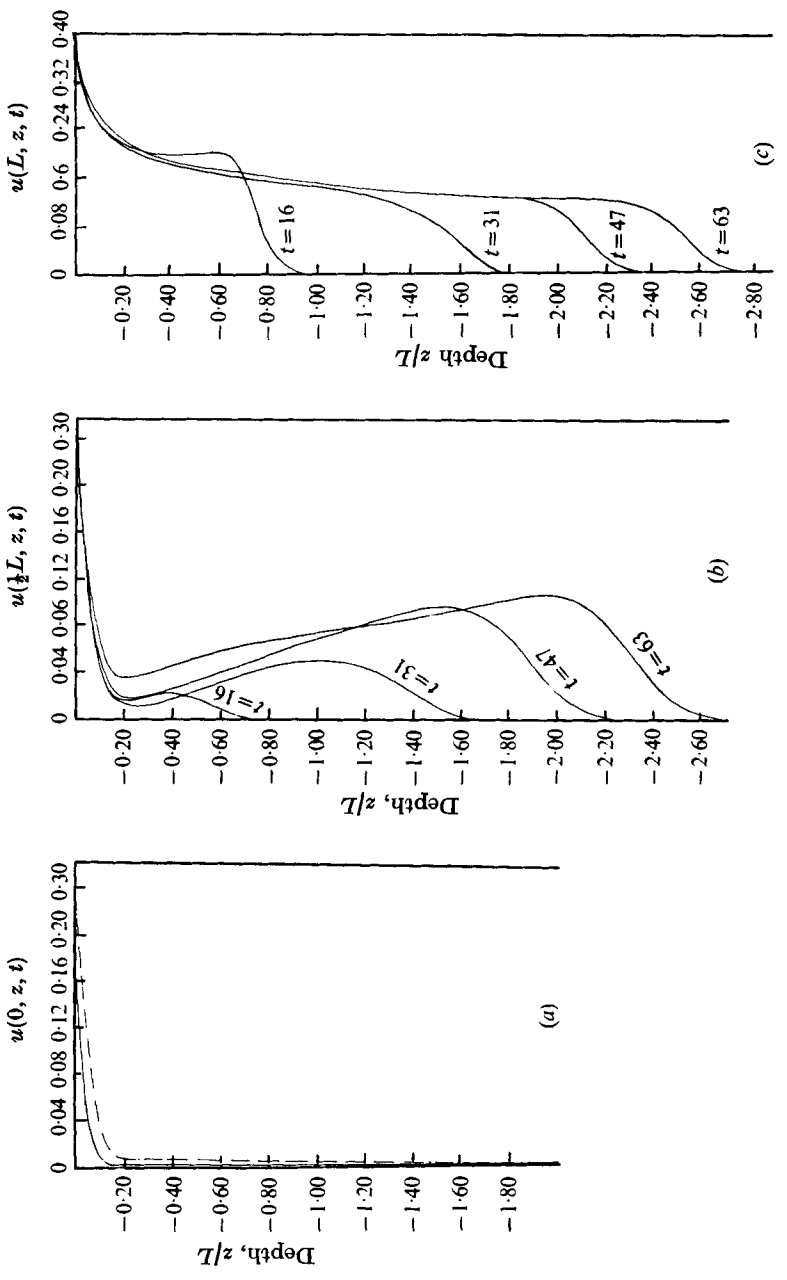

FIGURE 11. Profiles of the wind-directed current speed as a function of depth and time, for $\theta = 30°$ and $La = 0{\cdot}01$. The profiles are in planes at three spanwise stations. (*a*) Plane at $y = 0$, an upwelling location. (*b*) Plane through the centre of the cell. (*c*) Plane at $y = L$, a down welling location. —·—, $t = 16, 31$; —, $t = 63$.

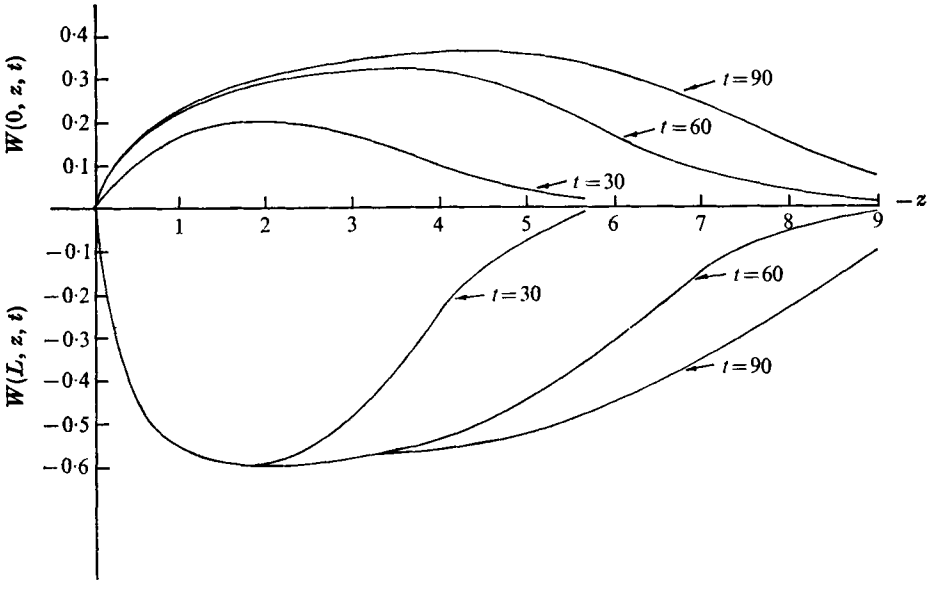

FIGURE 12. Vertical velocities as functions of depth at planes of convergence ($y = L$) and divergence ($y = 0$), for $\theta = 30°$, $La = 0{\cdot}01$ at various times.

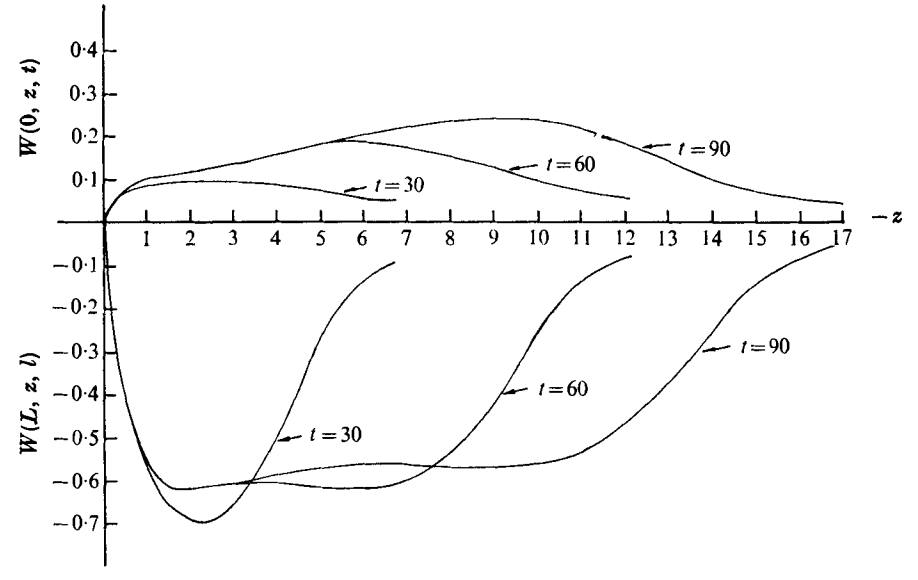

FIGURE 13. Vertical velocities as functions of depth at planes of convergence ($y = L$) and divergence ($y = 0$), for $\theta = 15°$, $La = 0{\cdot}01$ at various times.

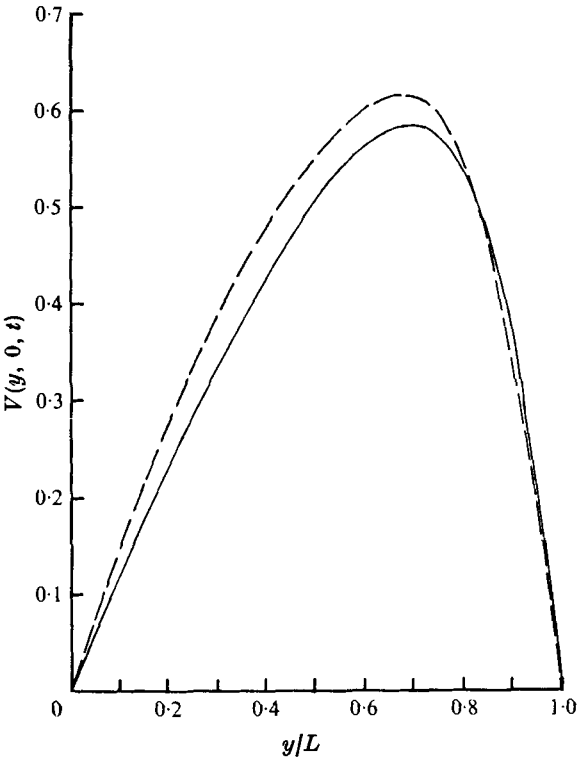

FIGURE 14. Surface values of the spanwise (sweeping) velocity component as a function of spanwise co-ordinate, for $\theta = 30°$, $La = 0{\cdot}01$, for $t = 30, 60, 90$. The curves for $t = 60$ and 90 are essentially coincident, so only one curve has been drawn for both time levels. —, $t = 30$; – – –, $t = 60, 90$.

5. Summary of the solutions and comparison with observations

5.1. *General features and surface wind-directed anomalies*

The solutions presented in §4 have the following features.

(i) The Langmuir cells are asymmetric, with downwelling speeds exceeding upwelling speeds typically by a factor of two or more. This factor falls below two only for large time.

(ii) Convergence zones occur along nodal lines of the simple surface-wave directional spectrum that is assumed. The wind-directed current component u has a sharp maximum above regions of downwelling. Away from the peak, the surface value of u varies gradually across the cell. Peak values of u typically exceed values away from the peak by 50–60 %.

(iii) The surface value of the horizontal velocity component that sweeps material towards convergence lines has approximately the same magnitude as the maximum value of the downwelling velocity component.

(iv) Current speeds for $\theta = 15°$ are generally slightly larger than those for $\theta = 30°$. This is consistent with the finding of CL that there appeared to be a (small) value of θ for which the Langmuir circulations are most intense.

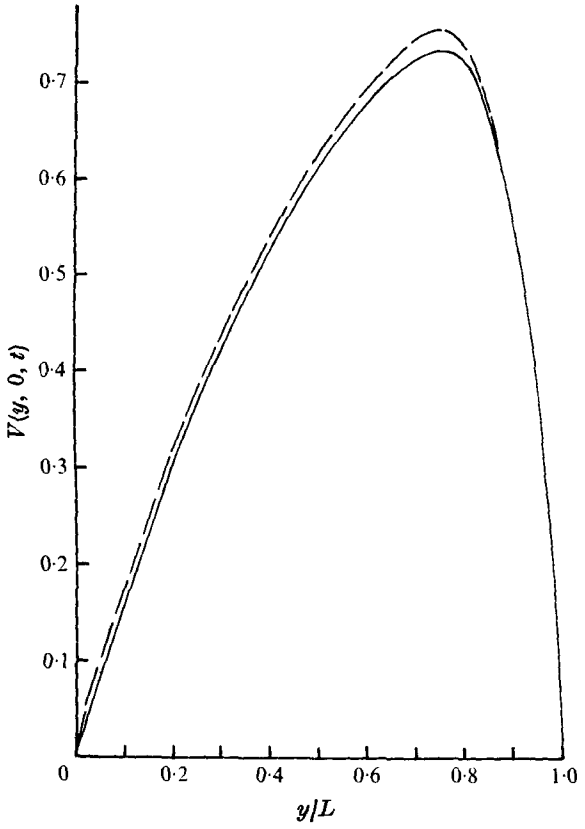

FIGURE 15. Surface values of the spanwise (sweeping) velocity component as a function of spanwise co-ordinate, for $\theta = 15°$, $La = 0{\cdot}01$, for $t = 30$, 60, 90. The curves for $t = 60$ and 90 are essentially coincident, so only one curve has been drawn for both time levels. – – –, $t = 30$; —, $t = 60$, 90.

(v) After an initial development period of about ten time units, the motions near the surface change very slowly with time.

Of the features listed in § 1, the first two are satisfied automatically, and the third is perfectly clear from the computed results, and so we do not need to consider these questions further.

The consideration of the fourth feature is complicated by the presence of the Stokes mass transport, and therefore will be considered in more detail below, while the fifth feature involves the typical magnitudes of the parameters appearing in the mean current decomposition (3), and this will also be dealt with in greater length below. Experimental features that have been reported but that do not have the same status as the five given in § 1 will also be discussed.

We start with the fourth feature. Experimental observations (e.g. Langmuir 1938 or Gordon 1970) indicate that flotsam, or dye, that concentrates in convergence lines tends to move faster than the surrounding fluid. The magnitude of this relative advancement of marked fluid has apparently never been measured. The visual method of determining the existence of relatively higher speeds in convergences amounts to an observation of a Lagrangian drift, and therefore includes both mean Eulerian currents, as calculated here, and the Stokes mass transport. According to Longuet-Higgins

(1953), therefore, the surface value of the total (dimensional) wind-directed transport will, in our case, be the sum

$$U_d = 2\epsilon^2 c \cos\theta[1 + \cos^2\theta \cos(\pi y/L)] + (u_*^2/\nu_T\kappa)\, u(y, 0, t), \tag{15}$$

where $c \equiv \sigma/\kappa$ is the characteristic phase speed of the surface wave field and $\epsilon = a\kappa$. The Stokes drift is least over convergence lines, while the second term, developed in response to the Langmuir cells, is greatest over convergence lines. The solutions reported for $u(y, z, t) - \bar{u}$ by CL are dominated by the first harmonic, and therefore vary with y essentially like $-\cos \pi y/L$. The location of the maximum of U_d was therefore determined by the sign of the coefficient of $\cos \pi y/L$ in (15), including the Stokes contribution and the contribution of u. From the calculations of the fully nonlinear equation developed here, however, the form of u is far from sinusoidal, and it is clear that local maxima of U_d necessarily occur at both convergence and divergence lines. The relative magnitudes of $u_*^2/\nu_T\kappa$ and of $\epsilon^2 c$ in (15) do not affect this conclusion. (We will show in the next subsection, however, that in typical cases U_d may be significantly larger in the convergence zones, and that the local maximum at divergence zones is a small effect.)

The observations that have been made suggest that satisfaction of this fourth feature requires only that U_d have a local maximum over downwelling regions. The relative advancement of material in the convergence zones should be most apparent once material has actually collected in these zones, since the region of divergence is soon cleared of visible traces of material. When attention is confined to the vicinity of the convergence zones, only a local maximum in the speed is likely to be revealed.

Thus, the first four qualitative features are confirmed by our calculations. The fifth, a quantitative statement, depends upon the parameters that occur in the theory. It will be seen from the next subsection that the computed results also compare favourably with this attribute.

5.2. *Quantitative comparisons*

In order to make quantitative assessments of the predicted current motions, it is necessary to fix the input parameters. The parameters involved are La, θ, and the scalings defined in equation (3): $u_*^2/\nu_T\kappa$, for x directed currents; and $u_*(\epsilon^2\sigma/\nu_T\kappa^2)^{\frac{1}{2}}$, for vertical and sweeping currents. (The parameter $(\epsilon^2\sigma/\nu_T\kappa^2)^{\frac{1}{2}}$ appears in the CL theory, where it is denoted by the symbol R.) To address these questions, we will first suppose that our solutions for $La = 0{\cdot}01$ are representative of situations of real interest, and that, as our solutions for $\theta = 15°$ and $\theta = 30°$ indicate, the current speeds are not sensitive functions of θ. Second, we will always have in mind a wind-generated wave field, and will employ empirical results for wind waves to estimate wave parameters when required. The object will be to relate all quantities in a rough way to the wind speed, since this is the only environmental parameter that is almost *always* reported by observers. The friction velocity can easily be related to the wind.

The most difficult parameter to estimate is ν_T. Three methods occur to us as ways to proceed: first, we can use the widely accepted results that the average surface drift is about 3·5 % of the wind speed U_w. Second, according to the data summarized by Scott *et al.* (1969) downwelling speeds are about 0·85 % of U_w. The reported downwelling speeds were certainly not maximum values, but should give a good idea of the correct orders of magnitude. We may therefore use this information to assign a value to ν_T by adjusting our downwelling speeds to $0{\cdot}0085U_w$. Third, the logarithmic structure of

the horizontal average $\bar{u}$ of u can be used to fix ν_T, as suggested in part 1. All three methods yield roughly similar results.

The estimate according to the first method follows from the horizontal average of the drift given by (15),

$$U_d = 2\epsilon^2 c \cos\theta + (u_*^2/\nu_T \kappa)\,\bar{u}(0,t). \tag{16}$$

Set $\bar{U}_d = 0{\cdot}035 U_w$, $\cos\theta \approx 1$, and $\bar{u} = 0{\cdot}3$, which is typical of the calculations in part 1. In a wind-generated sea, the wave height H (which in the present wave model is $4\epsilon/\kappa$), phase speed c, and wavenumber κ of waves corresponding to the peak of the wave energy spectrum depend upon the fetch and the wind duration in a complicated and poorly understood way. On the other hand, a simple relation to the wind seems to emerge for 'saturated' waves, or 'fully developed' seas. According to Stewart (1967), for example, for this case the dominant waves are characterized by

$$H \sim 0{\cdot}2 U_w^2/g, \quad c \sim U_w, \quad \sigma \sim g/U_w \tag{17a–c}$$

and, from these values,

$$\kappa \sim g/U_w^2. \tag{17d}$$

For fetch- or duration-limited situations, H and c are less than (17*a*) and (17*b*) indicate, and σ and κ are greater than (17*c*, *d*). Observations of Langmuir circulations have probably all been made under fetch- or duration-limited circumstances, but for purposes of estimating typical magnitudes in the absence of more specific data, the use of (17) seems reasonable. Adopting this course, we find

$$u_*^2/\nu_T \kappa = (\bar{U}_d - 0{\cdot}005 U_w)/\bar{u} = 0{\cdot}1 U_w. \tag{18}$$

As in part 1, we assume that the ratio of air to water friction velocities is about 30, and that the ratio of U_w to the air friction velocity is about 22. Then

$$U_w \approx 660 u_* \tag{19}$$

and the use of (17*d*) finally produces

$$\nu_T \approx 2{\cdot}3 \times 10^{-5} U_w^3/g. \tag{20}$$

As an example, for $U_w = 10$ m/s, this yields $\nu_T \approx 23$ cm^2/s, which seems like a plausible value.

The dimensionless maximum downwelling speed (the maximum of $|\bar{W}|$) in the present solution is about 0·6, leading to a corresponding dimensional downwelling speed of

$$w_d = 0{\cdot}6 \epsilon u_* (\sigma/\nu_T \kappa^2)^{\frac{1}{2}}. \tag{21}$$

To estimate ν_T by the second method, we set $w_d = 8{\cdot}5 \times 10^{-3} U_w$ (keeping the remarks already made about this value in mind) and find that

$$\nu_T \approx \epsilon^2 \sigma/87\kappa^2,$$

or, on replacing ϵ by wave height as before,

$$\nu_T \approx 7{\cdot}1 \times 10^{-4} H^2 \sigma. \tag{22}$$

(We note that this is the form of eddy viscosity invoked in the CL model. It is recovered here quite independently.) To reduce (22) to a function of U_w, we again use (17) to obtain

$$\nu_T \approx 2{\cdot}84 \times 10^{-5} U_w^3/g \tag{23}$$

which is remarkably close to the estimate (20) of the first method.

According to part 1, the slope of the logarithmic 'inertial sublayer' found numerically for $\bar{u}$ will agree with the experimentally measured value if

$$\nu_T \approx 0{\cdot}1 u_* k/\kappa,$$

where $k = 0{\cdot}4$ is von Kármán's constant. Using (17*d*) and (19), this produces

$$\nu_T \approx 6 \times 10^{-5} U_w^3/g. \tag{24}$$

The last value is higher than those from the previous two methods, but is of the same order of magnitude.

The first method leads to the following form for the Langmuir current vector $\mathbf{U}_c$ (from (3)):

$$\mathbf{U}_c \approx 0{\cdot}1 U_w \{u\mathbf{i} + \tfrac{1}{2}\kappa H \sqrt{10}(V\mathbf{j} + W\mathbf{k})\}. \tag{25}$$

To arrive at this form of $\mathbf{U}_c$, we have used only (17*b*) and (18).

We will now use (25) to estimate vertical and sweep speeds in the cells. With $H\kappa = 0{\cdot}2$ (as was found appropriate for saturated waves), the maximum downwelling speed is

$$0{\cdot}1 U \tfrac{1}{2} H\kappa \sqrt{10} \max |W| = 0{\cdot}019 U_w,$$

where $\max |W| \approx 0{\cdot}6$.

Thus, the maximum downwelling speed is twice the experimental values reported in the literature for downwelling. Since the maximum downwelling *must* exceed the reported values (which represent either some kind of average value over depth of the downwelling, or the downwelling very near the surface), this result is very reasonable (and our fifth feature is confirmed). Equation (25) also predicts a maximum sweeping speed of about $0{\cdot}02 U_w$, for $H\kappa = 0{\cdot}2$.

The x component of (25), together with the estimates which led to (25), show that the total surface drift U_d at convergence zones exceeds that at divergence zones by about 1 % of the wind speed. The local maximum over upwelling zones is relatively weak, exceeding the average total drift by only about 14 %; the local maximum over downwelling zones, on the other hand, exceeds the average total drift by about 30 %.

6. Concluding remarks

In parts 1 and 2 of this paper, a detailed picture of the Langmuir circulations and associated vertical momentum transport has been constructed. This picture is based upon a theory originating in earlier work by Craik & Leibovich (1976). The absence of a steady limit to the problem as formulated here results from the neglect of bottom friction and the neglect of Coriolis accelerations. Inclusion of either effect would permit the approach to a steady limit. Except for shallow basins, however, the time required for a steady limit to emerge probably greatly exceeds the lifetime of individual Langmuir cells. We contemplate a continuous process whereby Langmuir cells develop under given wind and wave conditions and disappear as the waves responsible for the non-uniform Stokes drift necessary to the theory detune, or as the wind direction shifts. According to the theory, the birth, life and death of a given cell requires at least several (perhaps 10 or more) units of the time interval T_d, which is typically of the order of minutes.

The circulations and wind currents that result from the present calculations seem to agree with the scant data available. Many open questions remain to be answered,

however, before the theoretical mechanisms explored here can be confirmed or disproved as an underlying explanation of Langmuir circulations. The most important questions that can be raised are those relating to the surface wave spectrum. In particular, are wind wave fields commonly associated with a structure with sufficient coherence to produce a spanwise varying Stokes drift? The present theory requires the waves to be phase locked, or nearly so, for a time interval of order T_d. (If the system is slightly detuned, Craik (1970) showed that the cells slowly drift perpendicular to the wind direction. Such a motion has been observed by Myer (1971).) This requirement is not conceptually restrictive, but whether it actually occurs in nature is open to question. (The effect of perspective on visual regularity of the sea surface is illustrated in interesting photographs in Kinsman (1965, p. 543). Kinsman remarks that the regular pattern that is apparently lost in a growing sea can be regained by shifting to a higher viewing level.) Recent calculations made by O. M. Phillips (private communication) indicate that the phase-lock time interval required here may be overly long, even for a bimodal wave spectrum.

Assuming, nevertheless, the existence of lines of maximum wave height, another question bearing further investigation is the location of convergence zones relative to lines of maximum wave height. According to the present theory, the waves that drive the Langmuir cells should have lines of maximum wave height midway between convergence zones (see figure 1). Myer (1971) has reported measurements that suggest that lines of maximum wave height exist, but that they coincide with convergence zones. This is a point that requires additional substantiation. From the presentation of Myer's data, wave records in the zones of maximum height seem to be between 5 and 8 wave periods in length. Without a very careful treatment of errors associated with the statistics, the significance of this data remains unclear.

The junior author is responsible for the development and implementation of the numerical procedures used in this work. The senior author is responsible for the other aspects of the work. A lively four-way correspondence with Dr A. D. D. Craik, Dr R. T. Pollard and Professor C. J. R. Garrett has been most stimulating and valuable to us. Although we do not necessarily agree with all of them on the explanation of Langmuir's circulations, we are grateful to them all for an exchange that has had a non-negligible impact on our own opinions. We would also like to thank Dr Craik for showing us his unpublished work on the instability mechanism for generating circulations, and Dr Pollard for showing us a draft of his forthcoming review of the Langmuir-circulation phenomenon. Professor K. E. Torrance has critically reviewed the numerical procedures described here, and we appreciate his advice. This work was supported by the National Science Foundation under Grant DES 74-13057 A01.

REFERENCES

Assaf, G., Gerard, R. & Gordon, A. L. 1971 Some mechanisms of oceanic mixing revealed in aerial photographs. *J. Geophys. Res.* **76**, 6550–6572.

Craik, A. D. D. 1970 A wave-interaction model for the generation of windrows. *J. Fluid Mech.* **41**, 801–821.

Craik, A. D. D. 1977 The generation of Langmuir circulations by an instability mechanism. *J. Fluid. Mech.* (in Press).

Craik, A. D. D. & Leibovich, S. 1976 A rational model for Langmuir circulations. *J. Fluid Mech.* **73**, 401–426.

EKMAN, V. G. 1905 On the influence of the Earth's rotation on ocean-currents. *Ark. Mat. Astr. Fys.* **2** (11), 1–52.

GAMMELSRØD, T. 1975 Instability of Couette flow in a rotating fluid and origin of Langmuir circulations. *J. Geophys. Res.* **80**, 5069–5076.

GARRETT, C. J. R. 1976 Generation of Langmuir circulations by surface waves – a feedback mechanism. *J. Mar. Res.* **34**, 117–130.

GORDON, A. L. 1970 Vertical momentum flux accomplished by Langmuir circulation. *J. Geophys. Res.* **75**, 4177–4179.

KINSMAN, B. 1965 *Wind Waves.* Prentice-Hall.

LANGMUIR, I. 1938 Surface motion of water induced by wind. *Science*, **87**, 119–123.

LEIBOVICH, S. 1976 On the evolution of the system of wind drift currents and Langmuir circulations in the ocean. Part 1. Theory and the averaged current. *J. Fluid Mech.* **79**, 715–743.

LEIBOVICH, S. & ULRICH, D. 1972 A note on the growth of small scale Langmuir circulations. *J. Geophys. Res.* **77**, 1683–1688.

LONGUET-HIGGINS, M. S. 1953 Mass transport in water waves. *Phil. Trans.* A, **245**, 535–581.

MYER, G. E. 1971 Structure and mechanism of Langmuir circulations on a small inland lake. Ph.D. dissertation, State University of New York at Albany.

PHILLIPS, O. M. 1966 *Dynamics of the Upper Ocean.* Cambridge University Press.

POLLARD, R. T. 1976 Observations and theories of Langmuir circulations and their role in near-surface mixing. Submitted to *Deep Sea-Res.*

ROACHE, P. J. 1972 *Computational Fluid Dynamics.* Alburquerque, N.M.: Hermosa Publishers.

SCOTT, J. T., MYER, G. E., STEWART, R. & WALTHER, E. G. 1969 On the mechanism of Langmuir circulations and their role in epilimnion mixing. *Limnol. Oceanog.* **14**, 493–503.

STEWART, R. W. 1967 Mechanics of the air–sea interface. *Phys. Fluids Suppl.* **10**, S 47–55.